RESEARCH ARTICLE

STRUCTURAL BIOLOGY

Reciprocal allosteric regulation of p38γ and PTPN3 involves a PDZ domain–modulated complex formation

Kai-En Chen,[1] Shu-Yu Lin,[1] Mei-Ju Wu,[1] Meng-Ru Ho,[1] Abirami Santhanam,[1] Chia-Cheng Chou,[1,2] Tzu-Ching Meng,[1,3]* Andrew H.-J. Wang[1,2,3,4]*

The mitogen-activated protein kinase p38γ (also known as MAPK12) and its specific phosphatase PTPN3 (also known as PTPH1) cooperate to promote Ras-induced oncogenesis. We determined the architecture of the PTPN3-p38γ complex by a hybrid method combining x-ray crystallography, small-angle x-ray scattering, and chemical cross-linking coupled to mass spectrometry. A unique feature of the glutamic acid–containing loop (E-loop) of the phosphatase domain defined the substrate specificity of PTPN3 toward fully activated p38γ. The solution structure revealed the formation of an active-state complex between p38γ and the phosphatase domain of PTPN3. The PDZ domain of PTPN3 stabilized the active-state complex through an interaction with the PDZ-binding motif of p38γ. This interaction alleviated autoinhibition of PTPN3, enabling efficient tyrosine dephosphorylation of p38γ. Our findings may enable structure-based drug design targeting the PTPN3-p38γ interaction as an anticancer therapeutic.

INTRODUCTION

Mitogen-activated protein kinases (MAPKs) are key regulators in the signaling pathways responsible for Ras-mediated oncogenesis. The role of the activation of the MAPKs extracellular signal–regulated kinase (ERK) and c-Jun N-terminal kinase (JNK) in promoting Ras transformation is clearly defined (*1*, *2*). In contrast, activation of p38 MAPKs suppresses of Ras transformation in human cancers through the inhibition of cell growth or enhancement of cell death (*3*, *4*). Furthermore, genetic ablation of the p38-specific activating kinases MAP kinase kinases (MKK3 and MKK6) enhances Ras-dependent tumorigenesis (*5*). The p38 MAPK family is composed of four isoforms: p38α, p38β, p38γ, and p38δ. All of the members in the p38 family are activated by the same upstream kinases (*6*). However, unlike other members of the p38 family, phosphorylation and activation of p38γ suppress Ras-induced oncogenesis (*7*, *8*). Ras activity increases the abundance of the nonphosphorylated form of p38γ, and depletion of p38γ limits the growth of Ras-transformed fibroblasts and Ras-mutant colorectal cancer (CRC) cells (*7–9*). Thus, these results indicate that p38γ-specific phosphatases may be involved in the oncogenic process directed by Ras signaling.

p38γ differs from other p38 MAPKs by the presence of a C-terminal ETPL motif, which binds to the PDZ domain in interacting proteins (*10*). PTPN3 (PTPH1), which is a member of the nontransmembrane 6 (NT-6) subfamily of the protein tyrosine phosphatase (PTP) superfamily, is a p38γ-interacting phosphatase (*11*). The PDZ domain of PTPN3 plays an important role in the robust tyrosine dephosphorylation of p38γ and subsequent increase of Ras-induced transformation (*11*), suggesting that PDZ domain–mediated binding to p38γ may be critical for the oncogenic activity of PTPN3. Moreover, increased protein abundance of p38γ and PTPN3 occurs in primary colon cancers, which have a high incidence of *KRAS* mutations (*7*, *11*, *12*), thus supporting the hypothesis that dephosphorylation of p38γ by PTPN3 could contribute to the transformative and invasive activity of Ras.

Most studies have focused on the dephosphorylation of MAPKs by phosphatases containing the "kinase interaction motif" (KIM-PTPs), including a group of dual specificity phosphatases (DUSPs) and a distinct subfamily, including HePTP, STEP, and STEP-like PTPs (*13–15*). Unlike KIM-PTPs that dock onto the KIM-binding site of substrates, PTPN3 likely interacts with the ETPL motif of p38γ through its PDZ domain (*11*), thus conferring specificity to the interaction between this phosphatase and p38γ. In addition to the PDZ-ETPL interaction, the catalytic domain of PTPN3 may bind to the kinase domain of p38γ (*11*). p38γ is fully active when dually phosphorylated on the Thr-Gly-Tyr (TGY) motif located in the activation loop, and the interaction with PTPN3 leads to tyrosine dephosphorylation of this motif, thereby inhibiting p38γ kinase activity (*11*).

To investigate the molecular mechanism of the interaction between PTPN3 and p38γ, we used a hybrid structural biology method. This analysis showed that, although the PDZ domain plays a key role in binding, the isolated catalytic PTP domain of PTPN3 is capable of forming a stable complex with p38γ. Using crystallography, we demonstrated the structural basis upon which PTPN3 recognizes dually phosphorylated p38γ, rather than monophosphorylated p38γ, as a substrate. This feature has not been reported in any of the previous structural studies of DUSPs or KIM-PTPs capable of dephosphorylating MAPKs, suggesting the basis for the specificity of the interaction between PTPN3 and p38γ. Furthermore, to determine the low-resolution solution structure of the PTPN3-p38γ active-state complex, we applied small-angle x-ray scattering (SAXS), which revealed how the catalytic cleft of the phosphatase and activation loop of the kinase are coordinated. Cross-linking coupled with mass spectrometry (MS) in conjunction with structural data illustrated that the PDZ domain confers rigidity to the PTPN3-p38γ complex. Finally, the PDZ domain had an intrinsic inhibitory characteristic that likely inhibits the phosphatase activity of PTPN3 in the absence of a substrate. Through the combination of hybrid structural biology methods, our study illustrated the mechanism of the allosteric regulation of p38γ by PTPN3, and thus provides the

[1]Institute of Biological Chemistry, Academia Sinica, Taipei 11581, Taiwan. [2]National Core Facility for Protein Structural Analysis, Academia Sinica, Taipei 11581, Taiwan. [3]Institute of Biochemical Sciences, National Taiwan University, Taipei 10717, Taiwan. [4]Graduate Institute of Translational Medicine, College of Medical Science and Technology, Taipei Medical University, Taipei 11047, Taiwan.
*Corresponding author. E-mail: tcmeng@gate.sinica.edu.tw (T.-C.M.); ahjwang@gate.sinica.edu.tw (A.H.-J.W.)

Downloaded from http://stke.sciencemag.org/ on February 5, 2015

potential for novel therapeutic interventions of p38γ-dependent transformation and oncogenesis.

RESULTS

PTPN3 and p38γ form a monomeric complex

To evaluate whether PTPN3 could form a stable binary complex with p38γ in solution, we generated constructs of human PTPN3 containing two substrate-trapping mutations, D811A and C842S. Previous studies have demonstrated that invariant Asp and Cys residues are catalytically essential for all PTPs and that their mutation would impair catalysis without affecting the substrate binding (*16*, *17*). We created two constructs: the elongated construct (amino acids 506 to 909) included the PDZ and PTP domains (N3PDZ-PTP), and the shorter construct (amino acids 628 to 909) contained only the PTP domain (N3PTP) (Fig. 1A and table S1). To generate a fully active, full-length p38γ for our study (Fig. 1A), we used a constitutively active mutant of MKK6 (hereinafter designated as $MKK6^{S207D/T211D}$) to phosphorylate Thr^{183} ($pThr^{183}$) and Tyr^{185} ($pTyr^{185}$) of p38γ in solution (hereinafter designated as phospho-p38γ) using previously described protocols (*18*). MS analysis demonstrated that the molecular weight of phospho-p38γ was 240 daltons larger than that of the unphosphorylated form (fig. S1, A and B), indicating the addition of three phosphate groups (PO_3). An analysis of the trypsin-digested peptides by MS showed that these three phosphorylation sites were Thr^{183} and Tyr^{185}on the TxY motif (fig. S1C), and Thr^{365} located in the C-terminal tail (fig. S1D). We did not observe phosphorylation of Ser^3 as reported previously (*10*, *18*), possibly because the specific construct and experimental condition used in our study favor the formation of phosphorylated Thr^{365} instead of Ser^3.

The mixture of N3PDZ-PTP with the D811A and C842S mutations (N3PDZ-$PTP^{D811A/C842S}$) and phospho-p38γ ($N3_{PDZ\text{-}PTP}$–p-p38γ complex) eluted from a Superdex 200 16/60 size exclusion chromatography (SEC) column at 73 ml (molecular weight, ~80 kD), different from the two individual proteins alone (Fig. 1B). The mixture of N3PTP with the D811A and C842S mutations (N3$PTP^{D811A/C842S}$) and phospho-p38γ ($N3_{PTP}$–p-p38γ complex) eluted at 75 ml, a position very similar

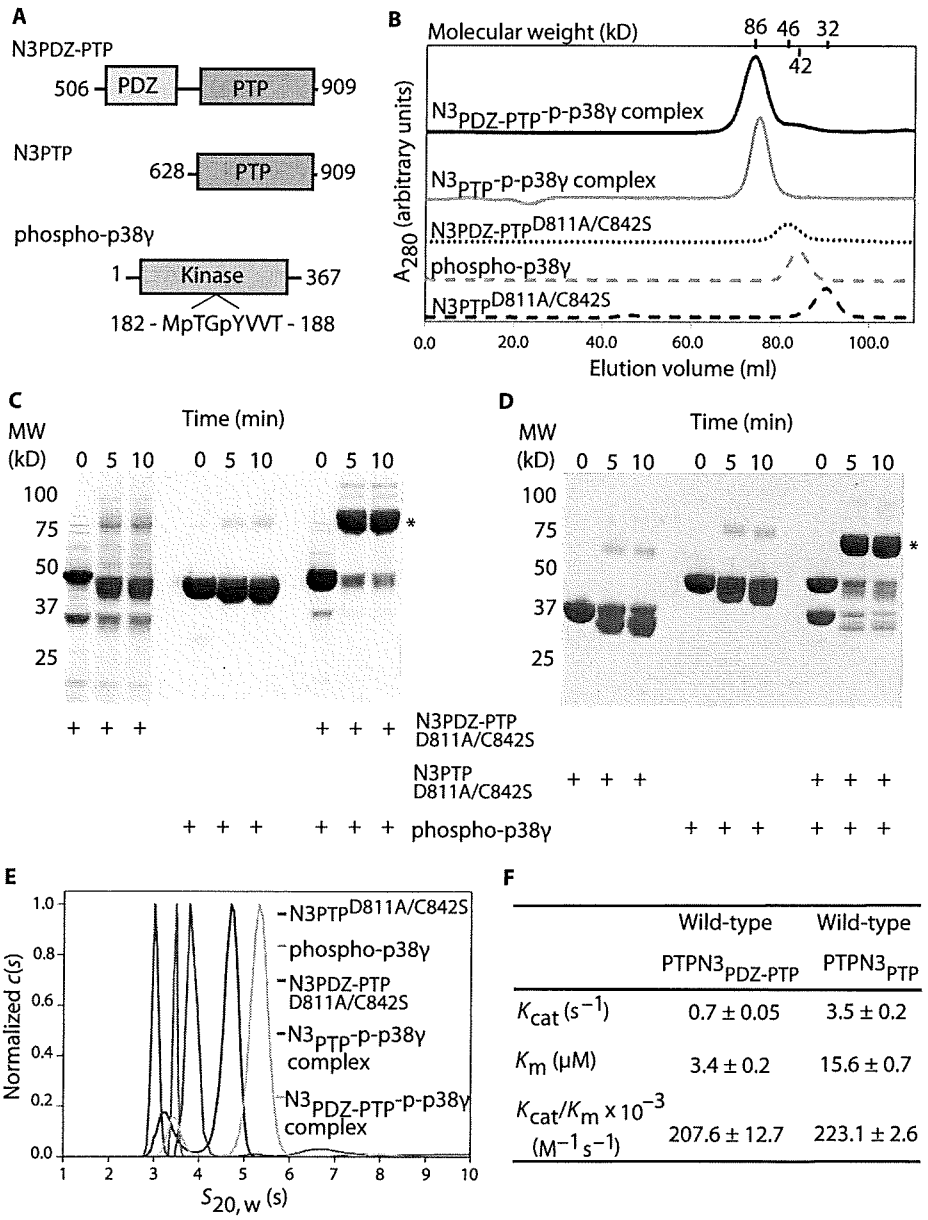

F

	Wild-type $PTPN3_{PDZ\text{-}PTP}$	Wild-type $PTPN3_{PTP}$
K_{cat} (s^{-1})	0.7 ± 0.05	3.5 ± 0.2
K_m (μM)	3.4 ± 0.2	15.6 ± 0.7
$K_{cat}/K_m \times 10^{-3}$ ($M^{-1}s^{-1}$)	207.6 ± 12.7	223.1 ± 2.6

Fig. 1. Details of PTPN3 and p38γ interaction. (A) Schematic showing the constructs of PTPN3 and p38γ used in this study. Synthetic peptide that mimics the TxY motif is indicated. (B) SEC profiles of the PTPN3 constructs, phospho-p38γ, and the complexes eluted at different position from a Superdex S200 16/60 column. Elution volumes of molecular mass standards are indicated at the top of the panel. (C and D) N3PDZ-$PTP^{D811A/C842S}$, N3$PTP^{D811A/C842S}$, and phospho-p38γ were cross-linked with BS3 for 0, 5, and 10 min at room temperature, revealing a monomeric species, whereas both $N3_{PDZ\text{-}PTP}$–p-p38γ and $N3_{PTP}$–p-p38γ reveal a 1:1 ratio complex (indicated by the asterisk). Cross-linked samples run faster than the non–cross-linked proteins on SDS–polyacrylamide gel electrophoresis (SDS-PAGE), because cross-linked proteins can form SDS complexes with a smaller Stokes radius than non–cross-linked protein: SDS complexes (*65*). (E) AUC sedimentation velocity experiment. Normalized *c*(*s*) distribution plots for the target constructs and the complexes. (F) Saturation kinetics using phospho-p38γ as a substrate. Data were fitted to the Michaelis-Menten equation and represent means ± SEM for at least three independent assays.

Downloaded from http://stke.sciencemag.org/ on February 5, 2015

to the elution volume of the $N3_{PDZ\text{-}PTP}$–p-p38γ complex (Fig. 1B), suggesting that the PTP domain alone could form a stable complex with phospho-p38γ. However, when mixed with unphosphorylated p38γ, $N3PTP^{D811A/C842S}$ eluted at 87 ml, consistent with a molecular weight of ~42 kD (fig. S2A), indicating that unphosphorylated p38γ and $N3PTP^{D811A/C842S}$ coeluted because of their similar masses, but did not form a stable complex.

We performed cross-linking reactions by adding the bis(sulfosuccinimidyl)suberate (BS3) cross-linker into protein mixtures in solution. In the presence of BS3, $N3_{PDZ\text{-}PTP}$–p-p38γ and $N3_{PTP}$–p-p38γ complexes were formed, which was revealed by the detection of cross-linked products with molecular weights of ~85 and ~75 kD, respectively (Fig. 1, C and D). As expected, the mixture of unphosphorylated p38γ and $N3PTP^{D811A/C842S}$ did not form a stable complex (fig. S2B), suggesting that the PTP domain of PTPN3 only recognized the active form of p38γ. To further characterize the interaction, we used analytical ultracentrifugation (AUC) to examine the oligomeric state of the $N3_{PDZ\text{-}PTP}$–p-p38γ and $N3_{PTP}$–p-p38γ complexes. Analysis of both complexes revealed a size that was consistent with an interaction of one N3PDZ-$PTP^{D811A/C842S}$ or $N3PTP^{D811A/C842S}$ with a phospho-p38γ monomer (Fig. 1E). Together, our results demonstrated that in the presence or absence of the PDZ domain, PTPN3 formed a complex with phospho-p38γ with a 1:1 stoichiometry.

Both the PDZ and PTP domains of PTPN3 regulate dephosphorylation of phospho-p38γ

We measured the phosphatase activity of the two PTPN3 constructs using phospho-p38γ as the substrate. In the presence of the PDZ domain, wild-type N3PDZ-PTP dephosphorylated phospho-p38γ with a K_m value of 3.4 μM and a K_{cat} of 0.7 s^{-1} (Fig. 1F). In contrast, without the PDZ domain, wild-type N3PTP dephosphorylated phospho-p38γ with a fivefold increase of K_{cat} and K_m compared to wild-type N3PDZ-PTP (Fig. 1F). These results suggested that the PDZ domain not only induced a strong binding of PTPN3 to phospho-p38γ but also reduced PTPN3-mediated catalysis of substrate dephosphorylation. Conversely, in the absence of the PDZ domain, wild-type N3PTP was sufficient to catalyze the dephosphorylation of phospho-p38γ with a robust efficiency, indicating that the PTP domain alone recognized dually phosphorylated p38γ as a substrate. Thus, the results from our kinetic study agreed with the cross-linking and AUC data that both wild-type N3PDZ-PTP and N3PTP could interact with phospho-p38γ for tyrosine dephosphorylation.

Structure of $N3PTP^{D811A/C842S}$–p-p38γ phosphopeptide complex reveals key features of the interaction

To elucidate the underlying molecular mechanism that causes the PTPN3-p38γ interaction and catalysis to occur, we solved the crystal structure of $N3PTP^{D811A/C842S}$ in complex with the dually phosphorylated p38γ peptide (amino acids 182 to 189) that mimics the TxY motif of the activation loop (Figs. 1A and 2A). This phosphopeptide complex structure was successfully determined at 2.5 Å, demonstrating a monomer in the asymmetric unit (Fig. 2A and Table 1). In general, the complex structure displayed a classic PTP fold, and residues Asp^{628} to Leu^{906} were clearly visible for refinement. Mapping of conserved residues onto the structure revealed that the dually phosphorylated p38γ peptide fit within a highly conserved catalytic cleft of $N3PTP^{D811A/C842S}$ (Fig. 2B). All six residues of the phosphopeptide were clearly delineated in the electron density map of the complex structure (Fig. 2A). The $pTyr^{185}$ (designated as P^{+0}) was buried deeply in the active-site pocket and surrounded by the highly conserved substrate-binding loops (Fig. 2C). A superimposition of the phosphopeptide complex structure with the wild-type N3PTP structure [Protein Data Bank (PDB) ID: 2B49] deposited from a structural genomics project revealed a high degree of similarity with an RMSD of 1.1 Å over 259 Cα atoms. The major difference occurred in the movement of the catalytic essential Trp-Pro-Asp–containing loop (WPD loop) from an open to a closed conformation (fig. S3, A and B). Moreover, the electron density of helix 1 was clearly defined in the phosphopeptide complex compared with the wild-type N3PTP structure (fig. S3C). We speculate that helix 1 could adopt a stable conformation in the presence of the phospho-p38γ substrate.

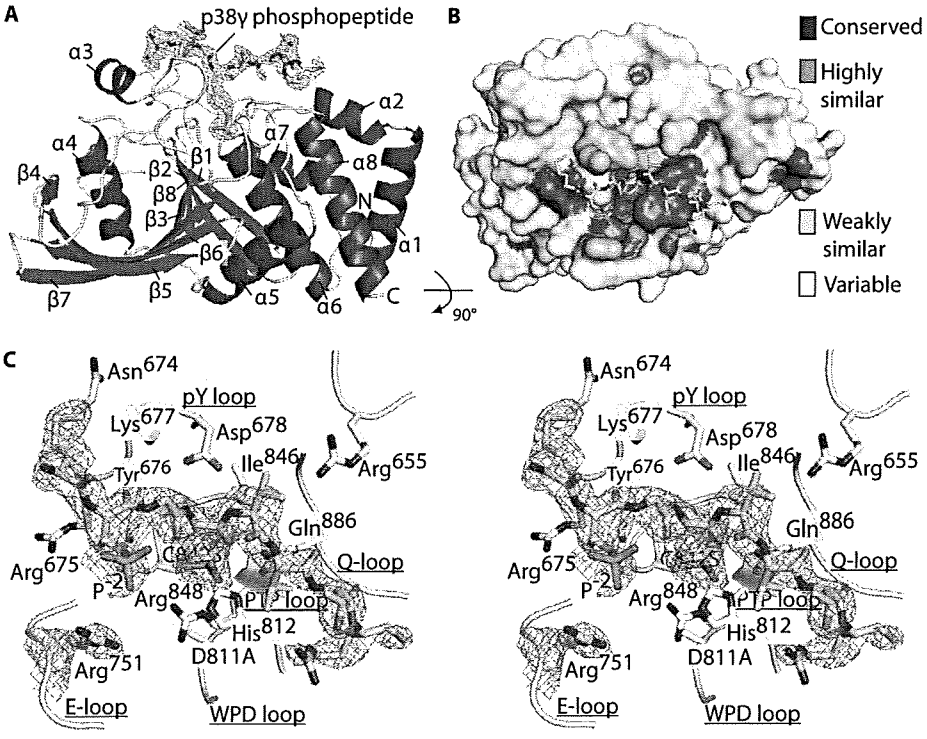

Fig. 2. Crystal structure of $N3PTP^{D811A/C842S}$ in complex with the dually phosphorylated p38γ peptide. (A) Representation of the phosphopeptide complex structure. The dually phosphorylated p38γ peptide is shown as a stick model. Electron density is shown in light blue. (B) Molecular surface of the phosphopeptide complex rotated 90° around the horizontal axis of (A) to show the sequence conservation among the FERM domain–containing PTPs. The surface is colored dark green, light green, wheat, and white to show residues that are conserved, highly similar, weakly similar, or variable, respectively, across the FERM domain–containing PTPs. (C) Stereo view of the complex structure highlights detailed interactions with the dually phosphorylated p38γ peptide. The electron density shown corresponds to that from a $2F_o - F_c$ map contoured at 1σ.

Downloaded from http://stke.sciencemag.org/ on February 5, 2015

Structural analysis reveals why dually phosphorylated p38γ is a preferred substrate of PTPN3

A unique feature in our structure was the salt bridge interaction between the phosphate oxygen of P^{-2} ($pThr^{183}$ in phospho-p38γ) and nitrogen atoms of the guanidine group of Arg^{751} in the E-loop of PTPN3 (Fig. 3A). The interaction of $pThr^{183}$ and Arg^{751} suggests that PTPN3 might prefer dually phosphorylated ($pThr^{183}$-Gly-$pTyr^{185}$) rather than monophosphorylated (Thr-Gly-$pTyr^{185}$) p38γ as a substrate. Indeed, kinetic analyses demonstrated that the K_m of wild-type N3PTP using monophosphorylated p38γ peptide is about 2.7-fold higher than that of the dually phosphorylated peptide substrate (Table 2). To further examine the critical role of Arg^{751} in conjunction with $pThr^{183}$, we generated an R751S mutant form of N3PTP ($N3PTP^{R751S}$), where the hydrogen bond required to maintain the salt bridge is lost. When incubated with the dually phospho-p38γ peptide, the observed K_m of $N3PTP^{R751S}$ was similar to that of wild-type N3PTP in complex with the monophosphorylated p38γ peptide (Table 2). Moreover, we observed that such salt bridge does not exist in the structure of HePTP in complex with a phosphorylated Erk2 peptide (Fig. 3B) (*19*, *20*) because Arg^{751} is not conserved in the E-loop of HePTP. Thus, these structural insights explain why phosphorylation of the Thr in ERK equivalent to Thr^{183} in p38γ is not necessary for substrate recognition by HePTP, which does not exhibit substrate preference between mono- and dually phosphorylated ERK (*19*, *20*). In contrast, the unique Arg^{751} and $pThr^{183}$ interaction likely plays an essential role in the recruitment of dually phosphorylated p38γ as a preferred substrate of PTPN3.

Table 1. Data collection and refinement statistics. RMSDs, root mean square deviations.

	4QUN	4QUM
Data collection statistics		
Construct used	$N3PTP^{C842S}$	$N3PTP^{D811A/C842S}$
With p38γ peptide	–	+
Space group	$C222_1$	$P3_121$
Wavelength (Å)	1.5400	1.0000
Resolution (Å)	50.00–1.86 (1.93–1.86)*	50.00–2.52 (2.60–2.52)*
Cell dimensions		
a, *b*, *c* (Å)	94.7, 97.0, 138.2	75.5, 75.5, 109.6
α, β, γ (°)	90.0, 90.0, 90.0	90, 90, 120
Total observations	362,451	59,306
Unique reflections	53,391	12,505
Completeness (%)	99.5 (100.0)*	98.0 (95.1)*
R_{merge}†	0.08 (0.88)*	0.122 (0.521)*
$<I/\sigma(I)>$	18.2 (2.2)*	10.79 (2.35)*
Multiplicity	6.8 (6.8)*	4.7 (4.0)*
Refinement statistics		
R_{work}/R_{free} (%)‡§	17.7/20.6	19.7/24.4
Number of protein atoms	4626	2312
Waters	355	43
Other	2 PO_4	1 peptide
Wilson B factor ($Å^2$)	31.9	41.1
Average B factor ($Å^2$)¶	35.2	35.5
Protein	35.1	25.3
Water	38.0	29.2
Ligand	26.0 (PO_4)	52.0 (peptide)
RMSDs		
Bond length (Å)	0.010	0.009
Bond angles (°)	1.26	1.25
Ramachandran plot	95.9% favored, 0.3% outlier	92.2% favored, 0.7% outlier

*Values in parentheses refer to the highest-resolution shell. †$R_{merge} = \Sigma|I - <I>|/\Sigma<I>$, where I is the intensity of each individual reflection. ‡$R_{work} = \Sigma h||F_o| - |F_c||/\Sigma|F_o|$, where F_o and F_c are the observed and calculated structure-factor amplitudes for each reflection h. §R_{free} was calculated with 10% of the diffraction data selected randomly and excluded from refinement. ¶Calculated using Baverage.

SAXS data reveal an active-state binding mode between N3PTP and phospho-p38γ

In addition to defining the exact binding interface of the activation loop of phospho-p38γ in the phosphopeptide complex structure, we used SAXS to investigate whether in solution, the $N3_{PTP}$–p-p38γ complex can support an active-state binding mode. Structural parameters such as the radius of gyration (R_g) and maximum linear dimension (D_{max}) of the complex were calculated using the SAXS profile, Guinier plot, and pair distance distribution plot (Fig. 4, A and B, and table S2). The pair distance distribution plot indicated that the $N3_{PTP}$–p-p38γ complex had a globular shape in solution, with a D_{max} of 91 Å and an R_g of 28.5 Å (Fig. 4B and table S2). Compared with other known SAXS-derived PTP-MAPK structures, we found that the R_g of the $N3_{PTP}$–p-p38γ complex was remarkably similar to the active-state complex of STEP and phospho-p38α (STEP–p-p38α complex) (table S3). Indeed, the ab initio structure of the complex, calculated using DAMMIN (*21*), revealed a high degree

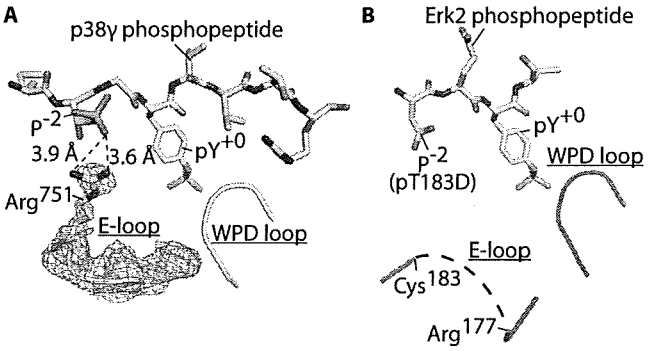

Fig. 3. Arg^{751} of PTPN3 plays a critical role in the interaction with $pThr^{183}$ of the dually phosphorylated p38γ peptide. (A) Active site of the phosphopeptide complex structure highlights the interaction (indicated as black dot line) between Arg^{751} on the E-loop and $pThr^{183}$ (P^{-2}). (B) Active site of HePTP in complex with the Erk2 mimetic peptide (PDB ID: 3D44). Missing residues on the E-loop of the HePTP structure are labeled as black dash line. The electron density shown corresponds to simulated-annealing OMIT $F_o - F_c$ map contoured at 3σ.

Table 2. Kinetic parameters of wild-type N3PTP using the p38γ phosphopeptides as a substrate.

Substrate	K_{cat} (s^{-1})	K_m (μM)	$K_{cat}/K_m \times 10^{-3}$ (M^{-1} s^{-1})
Wild-type N3PTP			
Dually phosphorylated p38γ peptide	19.9 ± 1.8	47.5 ± 6.3	420.9 ± 52.1
Monophosphorylated p38γ peptide	15.5 ± 0.2	126.0 ± 1.8	122.8 ± 3.3
$N3PTP^{R751S}$			
Dually phosphorylated p38γ peptide	20.1 ± 0.6	128.9 ± 6.2	155.9 ± 2.7

Downloaded from http://stke.sciencemag.org/ on February 5, 2015

of similarity with the active-state envelope of the STEP–p-p38α complex (Fig. 4, C and D). To generate an $N3_{PTP}$–p-p38γ complex, the PTP domain from our complex structure and phospho-p38γ (Fig. 2 and PDB code: 1CM8) were used as inputs for the FoXS calculation (*22*). Among the lowest-energy structures generated, one of the best-fit models ($\chi^2 = 2.3$) revealed a partial open conformation where the helix 4 of $N3PTP^{D811A/C842S}$ was bound to the C-lobe of phospho-p38γ (fig. S4A). The activation segments between the two proteins were in the same orientation, but too far apart to form a direct interaction. We speculate that this was likely a result of the unexpected orientation of the activation loop in the previously reported crystal structure of phospho-p38γ (*23*).

We noticed that the activation loop from the publicly available phospho-p38γ monomeric structure was hidden inside its activation cleft (*23*). In this particular orientation, $N3PTP^{D811A/C842S}$ was unable to bind to the activation loop of phospho-p38γ. For $pTyr^{185}$ to be accessed by the catalytic cleft of $N3PTP^{D811A/C842S}$, the activation loop must adopt an extended conformation away from its activation cleft. Several different deposited structures of phosphorylated (PDB code: 3PY3) and unphosphorylated p38 (PDB codes: 2OZA, 4EXU, and 4LOO) isoforms have revealed such extended conformation of their activation loops (*24–27*). To implement this feature onto phospho-p38γ, we modified the activation loop to two different extended conformations (one activation loop modeled toward the N-lobe and second one modeled toward the C-lobe) according to these available p38 structures (fig. S4B). The two example models of phospho-p38γ together with $N3PTP^{D811A/C842S}$ were used as inputs for the FoXS calculation (*22*). The optimized models generated from each input provided an excellent fit to the experimental SAXS data ($\chi^2 = 2.1$ and 2.0, respectively). Both models were globally similar (Fig. 4, E and F), and the catalytic cleft of $N3PTP^{D811A/C842S}$ localized on the bottom of the activation loop of phospho-p38γ (fig. S4C). The main difference between the two models was a ~25° shift of the $N3PTP^{D811A/C842S}$, depending on the orientation of the activation loop. Although both models provided an excellent fit to the SAXS data, the change in the orientation of $N3PTP^{D811A/C842S}$ could reflect its flexibility upon interaction with the activation loop of phospho-p38γ.

Cross-linking analysis defines a direct interaction between the PDZ domain of PTPN3 and the PDZ-binding motif of phospho-p38γ

Our SAXS data provided evidence that $N3PTP^{D811A/C842S}$ and phospho-p38γ form an active-state complex. Thus, we investigated whether the presence of the PDZ domain in PTPN3 induced a conformational change of the complex. We applied chemical cross-linking with BS3-d_0 (nondeuterated) and BS3-d_4 (deuterated) reagents and used liquid chromatography coupled with

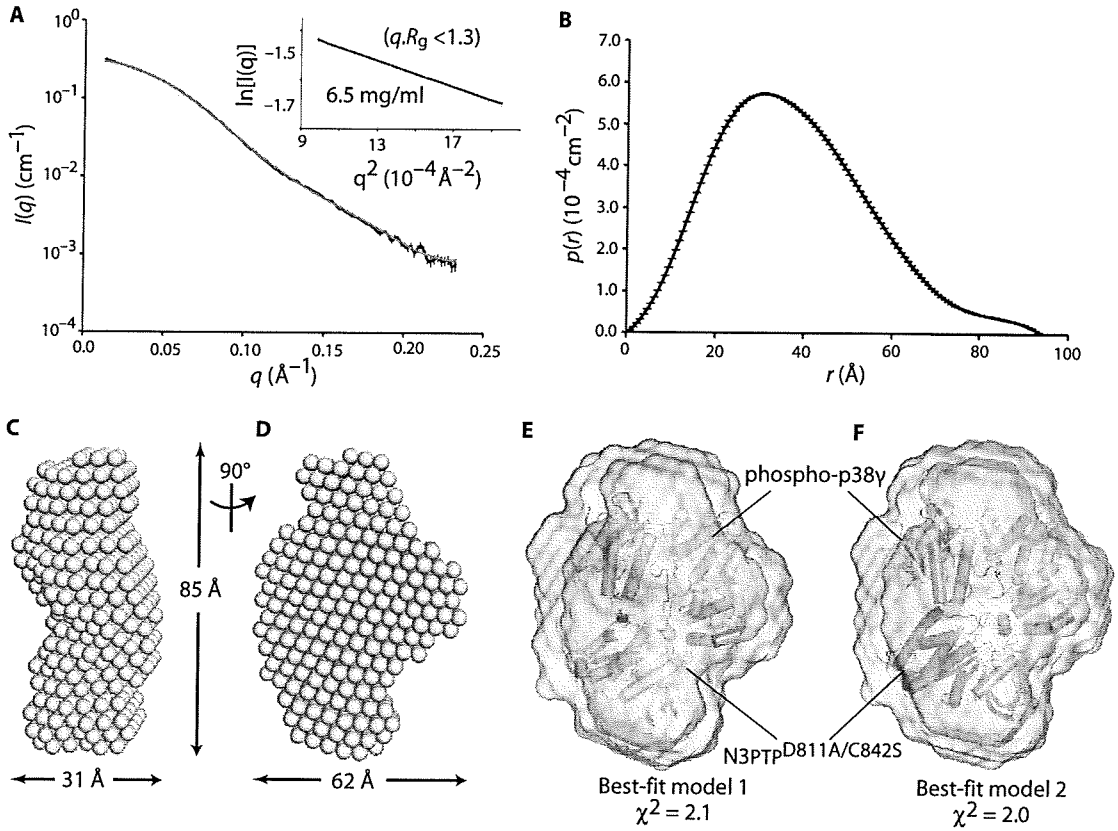

Fig. 4. SAXS data and ab initio model of the $N3_{PTP}$–p-p38γ complex. (A) Experimental SAXS scattering data of the $N3_{PTP}$–p-p38γ complex (black line) overlaid with the predicted scattering profile (red line) calculated from the ab initio model with the lowest χ value. Insert: Guinier plot at the low-angle region of the experimental scattering data ($q_{max} \times R_g < 1.3$). (B) Pair-distance distribution plots derived from the experimental scattering data using GNOM. (C) Probable shape of the $N3_{PTP}$–p-p38γ complex obtained by the averaging and filtering processed from the program DAMAVER. (D) SAXS-generated envelope rotated 90° around the vertical axis of (C). (E and F) Ab initio envelope (green cyan surface) overlaid with the optimized models of the $N3_{PTP}$–p-p38γ complex calculated from FoxS. The white envelope represents the total volume of the 10 aligned models obtained from the program DAMMIN.

Downloaded from http://stke.sciencemag.org/ on February 5, 2015

electrospray ionization MS (LC-ESI-MS) to map the $N3_{PDZ\text{-}PTP}$–p-p38γ complex. After manual inspection of the raw ESI-MS spectra, we identified 13 cross-linked peptides (table S4). Disregarding intramolecular cross-links, we detected six cross-linked pairs that connected N3PDZ-$PTP^{D811A/C842S}$ with phospho-p38γ (Fig. 5A, and fig. S5, A to F). Three lysine residues (Lys^{520}, Lys^{526}, and Lys^{532}) on the PDZ domain of N3PDZ-$PTP^{D811A/C842S}$ were linked to Lys^{352} and Lys^{363} on the C-terminal tail of phospho-p38γ (Fig. 5, A to C). To implement our cross-linked data into the structural context, we generated a model of the PTPN3 PDZ domain (hereinafter designated as N3PDZ) using the known structure of the PDZ domain of the PTPN3 homolog PTPN4 (PDB ID: 3NFK) as a template (fig. S6A) (*28*). On the basis of our model, three lysine residues of N3PDZ involved in cross-linking with phospho-p38γ were exposed to the surface and were positioned on the same interface as the conserved carboxylate-binding site (fig. S6, B and C), which plays a role in the interaction with the PDZ-binding motif (*28*).

Cross-linking analysis supports an active-state complex between PTPN3 and phospho-p38γ

In the interaction between the PTP domain of PTPN3 and phospho-p38γ, we identified two cross-linking pairs in both $N3_{PDZ\text{-}PTP}$–p-p38γ and

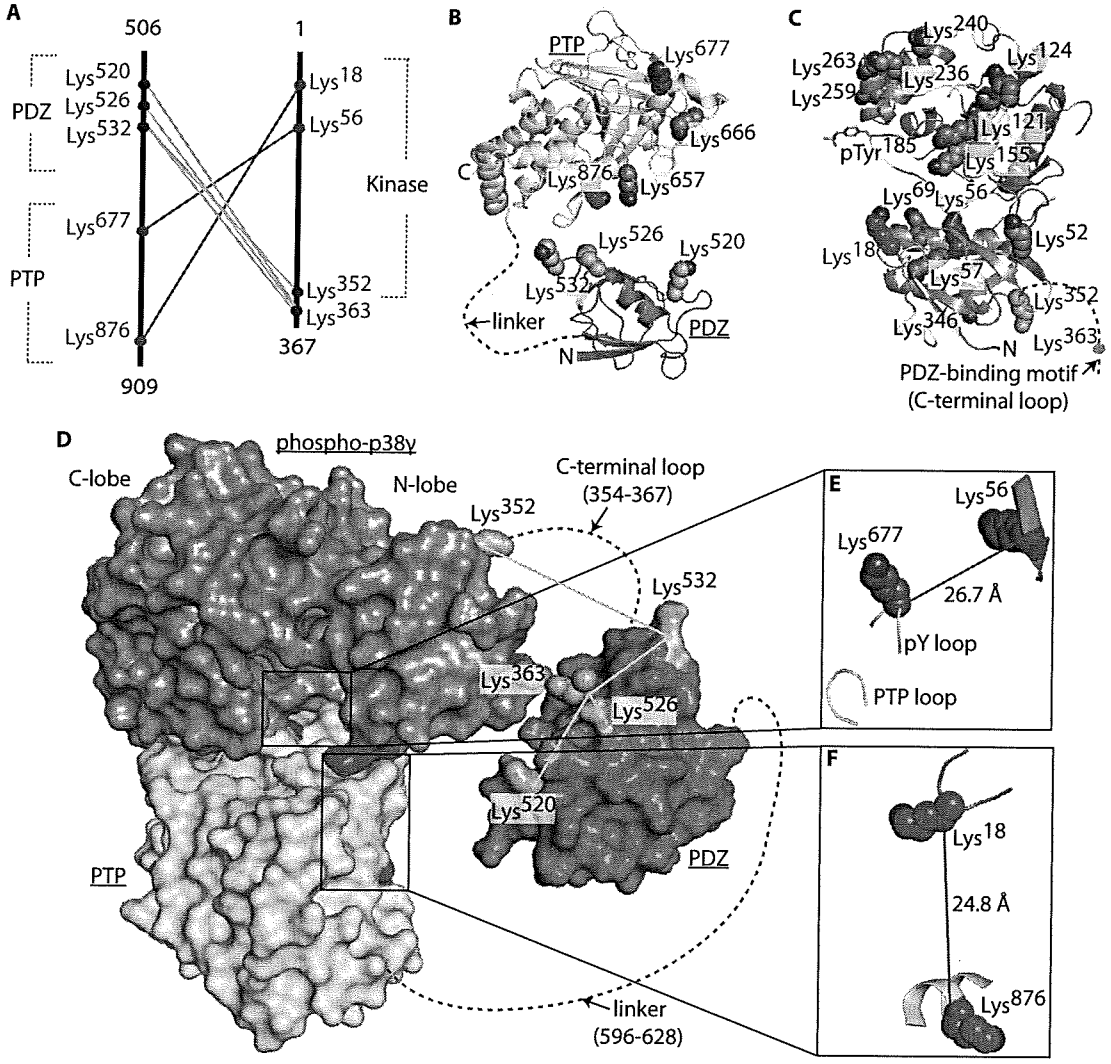

Fig. 5. Assembly of the $N3_{PDZ\text{-}PTP}$–p-p38γ complex with identified cross-links. (A) Cross-link map for N3PDZ-$PTP^{D811A/C842S}$ in complex with phospho-p38γ. Six observed intermolecular cross-linked peptides between N3PDZ-$PTP^{D811A/C842S}$ and phospho-p38γ are labeled as orange, blue, and green. (B and C) Representation of the PTP domain of the phosphopeptide complex structure combined with homology model of N3PDZ (B), and phospho-p38γ structures (PDB ID: 1CM8) with mapped intramolecular (red sphere) and intermolecular (orange, blue, and green sphere) cross-linked residues (C). The linker that connects the PDZ and PTP domains (Arg^{596} to Gly^{627}) and the C-terminal motif (Pro^{354} to Ser^{362}) of phospho-p38γ structure are both shown as color dot line. (D) Surface representation of the $N3_{PDZ\text{-}PTP}$–p-p38γ model complex with PDZ domain attached near the N-lobe of phospho-p38γ. The $N3_{PTP}$–p-p38γ complex was derived from the best-fit model 1 of SAXS. The cross-linked residues on PDZ and the PDZ-binding motif are labeled. For clarity, the PDZ-binding motif (Lys^{363} to Leu^{367}) was modeled using the complex structure of PTPN4 PDZ (PDB code: 3NFK) as a template. (E and F) Enlarged view showing the cross-linked pairs Lys^{677}-Lys^{56} (E) and Lys^{876}-Lys^{18} (F). The Cα distances of the observed lysine-lysine pairs are shown.

Downloaded from http://stke.sciencemag.org/ on February 5, 2015

$N3_{PTP}$–p-p38γ complexes (Fig. 5A and tables S4 and S5). By projecting these two pairs onto our crystal structure, we found that Lys^{677} and Lys^{876} were located on the surface of PTPN3 accessible to the solvent. In particular, Lys^{677} in PTPN3 was located on the phosphotyrosine recognition loop (pY loop) near the active-site pocket (Fig. 5B). Similarly, in phospho-p38γ, Lys^{18} and Lys^{56} were located on the N-terminal lobe adjacent to the activation loop (Fig. 5C). Using the two optimized $N3_{PTP}$–p-p38γ complex models derived from the SAXS analysis as a template (Fig. 5D and fig. S7A), we determined that the cross-linked pairs Lys^{677}-Lys^{56} and Lys^{876}-Lys^{18} were within the cross-linking distance limit for BS3 (permitted distance of Cα atoms is 27.4 Å) (*29*, *30*). In the SAXS-derived best-fit model 1, the linkage distances of Lys^{677}-Lys^{56} and Lys^{876}-Lys^{18} were 26.7 and 24.8 Å, respectively (Fig. 5, E and F). Similarly, both of the cross-linking pairs in model 2 were about 25 Å in length (fig. S7, B and C). Analysis of these cross-linking pairs suggests that the catalytic site of $N3PTP^{D811A/C842S}$ was in close proximity with the activation cleft of phospho-p38γ, which is consistent with the SAXS analysis.

Intermolecular cross-links define the PDZ domain arrangement in the active-state complex

The three lysines—Lys^{520}, Lys^{526}, and Lys^{532}—of the PDZ domain of $N3PDZ\text{-}PTP^{D811A/C842S}$ that were involved in the linkage were cross-linked to either Lys^{352} or Lys^{363} located on the ETPL motif of phospho-p38γ (Fig. 5D and table S4). In the absence of the PDZ domain in the $N3_{PTP}$–p-p38γ complex, we identified multiple intramolecular cross-links between Lys^{363} and three lysines located at different positions on the N-lobe of phospho-p38γ (Fig. 5C and table S5). These intramolecular cross-links did not occur in the $N3_{PDZ\text{-}PTP}$–p-p38γ complex (table S4). To model the position of the PDZ domain relative to phospho-p38γ in the $N3_{PDZ\text{-}PTP}$–p-p38γ complex, we used the cross-linked pair Lys^{532}-Lys^{352} as a guide. This model predicted that the PDZ domain was located near the N-lobe instead of the C-lobe of phospho-p38γ (Fig. 5D), suggesting that phospho-p38γ likely formed a more rigid conformation in the $N3_{PDZ\text{-}PTP}$–p-p38γ complex and providing evidence for how the PDZ domain interacts with p38γ during PTPN3-mediated dephosphorylation.

Cross-linking analysis defines an autoinhibitory characteristic of the PDZ domain in PTPN3

We did not observe intramolecular cross-links between the PDZ and the PTP domains of PTPN3 in the $N3_{PDZ\text{-}PTP}$–p-p38γ complex. To gain additional insights into the spatial relationship between these two domains, we cross-linked the $N3PDZ\text{-}PTP^{D811A/C842S}$ monomer in the absence of phospho-p38γ. We found that Lys^{876} in the PTP domain was cross-linked to Lys^{526} in the PDZ domain (fig. S5G and table S6), suggesting that the PDZ and PTP domains likely formed an intramolecular interaction in the absence of a substrate. In other contexts, direct protein interaction was found to be required for cross-linking to occur (*29*). Using the information from the cross-linking experiment to constrain the simulated docking of the PDZ and PTP domains using HADDOCK (*31*, *32*) generated 189 structures in four clusters (fig. S8, A to D). In each cluster, the PDZ domain was bound to the interface between helices 2 and 7 of the PTP domain. From the lowest energy structure generated by HADDOCK (Fig. 6, A and B), the two domains rearranged to form a compact conformation (Fig. 6A). This suggests that $N3PDZ\text{-}PTP^{D811A/C842S}$ was likely to be in an autoinhibitory conformation where the catalytic cleft of the PTP domain was blocked through allosteric regulation by its PDZ domain. To test this hypothesis, we measured the activity of two wild-type PTPN3 constructs using para-nitrophenyl phosphate (*p*NPP) as a substrate (*33*). Our results showed that wild-type N3PDZ-PTP had much lower activity compared to wild-type N3PTP (Fig. 6C). The cross-linking–based model of PTPN3 together with the kinetic analysis of phospho-p38γ (Fig. 1F) suggests that the PDZ and PTP domains of PTPN3 undergo a profound spatial rearrangement to form an open conformation upon substrate binding, thus restoring its phosphatase activity toward phospho-p38γ and potentially other similar PDZ-binding substrates (Fig. 6D).

DISCUSSION

We investigated the architecture of the PTPN3–p-p38γ complex using a generic hybrid structural biology method. Given the fact that PTPN3

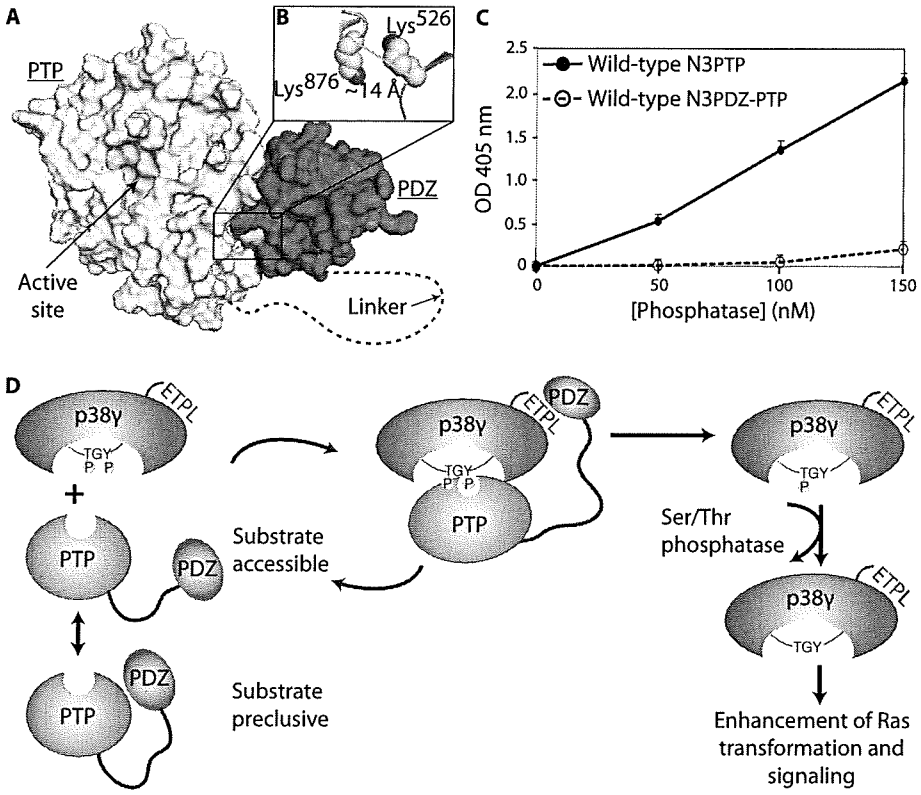

Fig. 6. Intrinsic inhibitory characteristic of the PDZ domain of PTPN3. (A) Surface representation of the lowest-energy HADDOCK structure of $N3PDZ\text{-}PTP^{D811A/C842S}$ to show the close proximity of the PDZ and PTP domains. The linker that connects the two domains is also shown. (B) Enlarged view showing the cross-linked pair Lys^{526}-Lys^{876}. The Cα distance of observed lysine-lysine pair is shown. (C) *p*NPPase activity of wild-type N3PDZ-PTP (dashed line) and N3PTP (solid line) to show the regulatory role of the PDZ domain. Data represent means ± SE of the mean for at least three independent assays. (D) Schematic showing PTPN3-mediated dephosphorylation of phospho-p38γ to induce Ras transformation. Tyrosine and threonine dephosphorylation steps are highlighted with red arrows.

Downloaded from http://stke.sciencemag.org/ on February 5, 2015

belongs to the subtype of nontransmembrane classical PTPs without a KIM or a kinase interaction sequence (KIS), it should exhibit a unique structural feature in recognizing phospho-p38γ as a substrate. Our results showed that the PTP domain of PTPN3 is sufficient to form an active-state complex with the fully activated p38γ. In the presence of the PDZ domain, PTPN3 forms a similar active-state complex with phospho-p38γ, suggesting that the PDZ domain, although important for binding to the C-terminal ETPL motif of phospho-p38γ, does not alter the interaction between the phosphatase and the kinase domains during catalysis. We also demonstrated that a direct contact between the PDZ and PTP domains was important for switching off the phosphatase activity of PTPN3 in the absence of phospho-p38γ, thus illustrating a role of the PDZ domain in intramolecular allosteric inhibition of PTPN3.

Our study of the PTPN3–p-p38γ complex revealed a distinct structural feature that renders dually phosphorylated p38γ susceptible to substrate recognition by PTPN3. Unlike the disordered E-loop in KIM-containing PTPs (*34*), the E-loop of PTPN3 is well ordered and stabilized through a hydrogen bond interaction between Arg^{751} and $pThr^{183}$ of phospho-p38γ. Because of the presence of Arg^{751}, dually phosphorylated, but not monophosphorylated, p38γ is coordinated well with the catalytic cleft of PTPN3. Sequence alignments indicated that the E-loop in all KIM-containing PTPs is one residue shorter than PTPN3 and its subfamily members (fig. S9). Collectively, our structural data suggest that PTPN3 along with other members in the same subfamily may only recognize fully activated MAPKs for tyrosine dephosphorylation of the activation loop. On the other hand, KIM-containing PTPs show no preference in dephosphorylation of both dually phosphorylated and monophosphorylated MAPKs. We propose that such unique substrate specificity determined by the rigidity of the E-loop and presence or absence of Arg^{751} between two subtypes of PTPs may play a key role in the regulation of MAPK-dependent signal transduction. Additional experiments are required to reveal their distinct functions under various pathophysiological conditions.

The specificity of PTPN3 toward dually phosphorylated substrate suggests that the product of the first step of catalysis is likely to be dephosphorylation of $pTyr^{185}$ of phospho-p38γ (Fig. 6D). For complete dephosphorylation, a serine and threonine phosphatase is needed to remove the phosphate from Thr^{183} of phospho-p38γ (Fig. 6D). Protein phosphatase 2A (PP2A), which dephosphorylates other MAPKs (*35*), is a possible candidate to dephosphorylate Thr^{183} of phospho-p38γ. PP2A has a much higher efficiency to dephosphorylate phosphothreonine in the activation loop of ERK2 once the phosphate had been already removed from the tyrosine residue compared to the dually phosphorylated substrate (*36*). Although it is not known whether PP2A can recognize p38 MAPKs as substrates, PTPN3 and PP2A may act sequentially to dephosphorylate and thereby completely inhibit the kinase activity of phospho-p38γ. Moreover, these two phosphatases may function synergistically to dephosphorylate phospho-p38γ in the signaling pathway that promotes Ras transformation.

The PDZ domain of PTPN3 interacts with the ETPL motif of p38γ (*11*), and we found that the PTP domain of PTPN3 interacts with the activation loop of p38γ. The PDZ domain may first recruit phospho-p38γ, but not other p38 isoforms or MAPKs without a PDZ-binding motif, to form a complex with PTPN3. This interaction likely stabilizes the position of the PDZ domain on the surface of N-lobe of phospho-p38γ, thus lifting the autoinhibitory constraint of PTPN3 and rendering the PTP domain openly accessible to the dually phosphorylated activation loop of phospho-p38γ (Fig. 6D). Second, interaction of the PDZ domain with the PDZ-binding motif promotes a compact complex formation between the PTP domain and the kinase domain (Fig. 6D), thus facilitating the efficiency of PTPN3-dependent tyrosine dephosphorylation of phospho-p38γ. After dephosphorylation, p38γ likely dissociates from PTPN3, enabling the PDZ domain to interact with the PTP domain, forming an inhibitory conformation (Fig. 6D). PTPN4 has high sequence and structural similarity in both PDZ and PTP domains with PTPN3, suggesting that this mechanism may also apply to the regulation of PTPN4 catalytic activity. Thus, the structural features elucidated by our study illustrate a potentially conserved role of PDZ domain in allosteric regulation of PTP activity, substrate recruitment, and substrate dephosphorylation during a dynamic process.

In addition to p38γ, the ephrin family of receptor tyrosine kinases (EphRs) are another large group of kinases containing a PDZ-binding motif located at the C terminus (*37*). EphRs and ephrin ligands form an important intercellular cell communication system in normal and disease states (*38*). The fourth PDZ domain of PTPN13, a member of the FERM-containing PTP subfamily, is critical for PTP13-dependent tyrosine dephosphorylation of EphR-B1 (*39*), thus illustrating a potential role for the PDZ domain of PTPN13 in substrate recruitment. Several EphRs, including EphR-A1, EphR-A2, EphR-B2, and EphR-B4, are abundant in CRC (*40*, *41*). Because PTPN3 is also abundant in CRC (*11*), a possible involvement of PTPN3-dependent dephosphorylation of EphRs in the context of CRC is suggested. The significance of such regulatory process and its contribution to the development of CRC require further investigation, including in-depth structural analyses.

In conclusion, our findings suggest two new approaches for rational drug design to target cancers, especially CRC, in which PTPN3 is highly expressed and expected to promote Ras oncogenic signaling through dephosphorylation of phospho-p38γ (*11*). First, an allosteric inhibitor designed to lock the PDZ and PTP domains together would inhibit PTPN3. A related allosteric inhibitor of PTPs was designed to target the C-terminal disordered segment of PTP1B to inhibit tumor growth in a HER2-positive mouse model (*42*). Second, an inhibitor designed to disrupt the interaction between the PDZ domain of PTPN3 and the PDZ-binding motif of phospho-p38γ would suppress efficient dephosphorylation of phospho-p38γ from PTP-substrate complex formation. Thus, our study not only elucidates the molecular basis of PTPN3–p-p38γ interactions but also sheds light on potential new therapeutic strategies for cancer.

MATERIALS AND METHODS

Cloning of PTPN3 and p38γ constructs

Polymerase chain reaction (PCR) fragments of N3PDZ-PTP and N3PTP were amplified from a full-length human PTPN3-encoded gene. PCR fragments of p38γ and constitutively active mutant, S207D and T211D, of $MKK6^{1–334}$ were amplified from the full-length human p38γ and human MKK6, respectively. All amplified gene products were ligated into an N-terminal His-tag pMCSG7 vector using ligation-independent cloning except for N3PDZ-PTP, for which an N-terminal His–GST (glutathione *S*-transferase)–tag pMCSG10 vector was used (*43*).

Site-directed mutagenesis

All mutants of N3PDZ-PTP and N3PTP were generated using the QuikChange Site-Directed Mutagenesis protocol following the manufacturer's instructions (Stratagene). The forward primers used in this study, with the mutated codon underlined, were as follows: $N3PTP^{R751S}$, 5′-CTCTCACAGAACGAGGGAGCACCAAATGTCACCAGTAC-3′; $N3PDZ\text{-}PTP^{D811A}$ and $N3PTP^{D811A}$, 5′-GTACGTCGCATGGCCTGCCCACGGTGTGC-3′; $N3PDZ\text{-}PTP^{C842S}$ and $N3PTP^{C842S}$, 5′-CCCGTCCTAGTTCACAGCAGTGCTGGAATAG-3′; $MKK6^{S207}$, 5′-CAGTGGCTACTTGGTGGACGATGTTGCTAAAACAATTGATG-3′; $MKK6^{T211D}$, 5′-GGTGGACGATGTTGCTAAAGATATTGATGCAGGTTGCAAAC-3′. All of the mutations were confirmed using DNA sequencing and are summarized in table S1.

Downloaded from http://stke.sciencemag.org/ on February 5, 2015

Protein expression and purification

All of the His-tagged constructs were expressed in *Escherichia coli* BL21 (DE3) cells at 37°C, except for His-GST–tagged N3PDZ-PTP, for which *E. coli* BL21–CodonPlus (DE3)–RIL cells were used. Protein expression was induced by the addition of IPTG (isopropyl-β-D-thiogalactopyranoside) to a final concentration of 1 mM at an OD_{600} (optical density at 600 nm) of 0.5. The temperature was then reduced to 18°C overnight. Cell pellets were lysed in 50 ml (per liter of culture) of lysis buffer consisting of 50 mM tris-HCl (pH 7.5), 500 mM NaCl, 5% glycerol, and protease inhibitor cocktail tablet, EDTA-free (Roche). The lysate was centrifuged at 20,000 rpm for 30 min using a JA 25.5 rotor in an Avanti J-25I centrifuge (Beckman Coulter) to separate the soluble supernatant from the insoluble cell pellet. Metal affinity chromatography was performed according to previously described protocols (*44*).

After metal affinity purification, 1 mg of tobacco etch virus (TEV) protease was added per 50 mg of eluted protein to remove the N-terminal tag from the target constructs. The mixture was dialyzed overnight in a 3500-dalton molecular weight cutoff membrane tubing (Pacific Laboratory) against 3 liters of dialysis buffer consisting of 50 mM tris-HCl (pH 7.5), 500 mM NaCl, 5% glycerol, and 0.5 mM TCEP at 4°C. After dialysis, cleaved and uncleaved proteins were separated using reverse metal affinity chromatography. The flow-through containing the His-tag–cleaved protein was collected and further purified using SEC. For SEC, the protein was eluted either from a Superdex 200 16/600 or a Superdex 75 16/60 column (Amersham Biosciences) equilibrated with a buffer containing 50 mM tris-HCl (pH 7.5), 150 mM NaCl, and 10 mM freshly prepared DTT (dithiothreitol) as described previously (*45*). The purity and integrity of purified protein were analyzed by SDS-PAGE. Protein concentrations were determined using a NanoDrop ND-1000 spectrophotometer (Thermo Scientific) at 280 nm.

In vitro phosphorylation of p38γ

Activation of p38γ was performed similar to the one described previously (*18*, *23*). Typically, 15 mg of purified p38γ at 0.5 mg/ml was added into an activation buffer containing 250 mM tris-HCl (pH 7.5), 5 mM $MgCl_2$, 5 mM $MnCl_2$, 10 mM ATP (adenosine 5′-triphosphate), and the constitutively active mutant of MKK6 at 20 μg/ml. After 30 min of incubation at 30°C, the sample was concentrated to 5 ml and applied to a Mono Q 5/50 GL column (Amersham Biosciences) equilibrated in buffer containing 50 mM tris-HCl (pH 7.5). The sample was eluted with a 0 to 500 mM NaCl gradient and, finally, purified by SEC on a Superdex 200 16/60 column containing 50 mM tris-HCl (pH 7.5), 150 mM NaCl, and 2 mM DTT (Amersham Biosciences). The phosphorylation site of p38γ was confirmed by tryptic digestion and MS.

Analytic ultracentrifugation

Sedimentation velocity analysis was performed with an XL-A analytical ultracentrifuge (Beckman Coulter) with absorption optics, using an AnTi60 rotor. Control reference buffer and samples in 50 mM tris-HCl (pH 7.5), 150 mM NaCl were added to double-sector centerpieces and spun at 45,000 rpm for 18 hours at 20° or 4°C. Detection of concentrations as a function of radial position and time was performed by optical density measurements at a wavelength of 280 nm, with absorbance profiles recorded every 3 min. The buffer density and viscosity were calculated using the software SEDNTERP (*46*), and the data were analyzed using SEDFIT software (*47*). The plot of the AUC profiles was made with the software GUSSI (http://biophysics.swmed.edu/MBR/software.html).

Chemical cross-linking

The purified N3PDZ-PTP$^{D811A/C842S}$, N3PTP$^{D811A/C842S}$, p38γ, and phospho-p38γ mixtures in 50 mM Hepes (pH 7.5), 150 mM NaCl were concentrated to 40 μM. For cross-linking, 5 μl of a 4 mM BS3-d_0/d_4 cross-linker (1:1 ratio of d_0:d_4 analogs) in dimethyl sulfoxide (DMSO) (Thermo Fisher Scientific) was mixed with 50 μl of each sample. The optimized ratio of cross-linker to protein was empirically determined. Once the BS3-d_0/d_4 cross-linker was added, the reaction was performed as previously described (*48*). The reaction was quenched by addition of freshly prepared 20 mM ammonium bicarbonate (pH 8.5), and the cross-linked products were analyzed by SDS-PAGE.

Tryptic digestion

Target bands from the SDS-PAGE gels were excised and reduced with 55 mM dithioerythritol (DTE) in 25 mM $(NH_4)HCO_3$ (pH 8.5) for 1 hour at 37°C, and then alkylated with 100 mM iodoacetamide for 1 hour in the dark at room temperature. Alkylated samples were digested with trypsin (Promega) overnight using an enzyme-to-substrate ratio of 1:100 (w/w) at 37°C. The digested sample was stopped by adding 0.1% formic acid (FA) and analyzed by liquid chromatography electrospray ionization tandem MS (LC-ESI-MS/MS).

Liquid chromatography electrospray ionization tandem MS

Peptide samples were reconstituted in buffer A (0.1% FA in H_2O) and analyzed on Waters SYNAPT G2 High Definition Mass Spectrometry (Waters). Samples were injected onto a 2-cm × 180-μm capillary trap column and separated on a 75-μm × 25-cm nanoACQUITY 1.7-μm BEH C18 column using a nanoACQUITY Ultra Performance LC system (Waters). The column was maintained at 35°C, and bound peptides were eluted with a gradient of 5 to 40% buffer B [buffer A, 0.1% FA in H_2O; buffer B, 0.1% FA in acetonitrile (ACN)] for 30 min. The MS was operated in ESI positive V mode with a resolving power of 10,000 and calibrated with a synthetic human [Glu1]-Fibrinopeptide B solution (0.5 pmol/ml; Sigma-Aldrich) delivered through the NanoLockSpray source. Data acquisition was performed with data-directed analysis (DDA) method. The DDA method included one full MS scan [mass/charge ratio (*m/z*) 350 to 1600, 1 s per scan] and three MS/MS scans (*m/z* 100 to 2000, 1 s per scan) performed sequentially on the three most intense ions present in the full scan mass spectrum. The MS and MS/MS raw data were converted into peak lists using ProteinLynx Global SERVER 2.5 (Waters). Analysis of all MS/MS samples was performed with Mascot (Matrix Science; version 2.4.0). Mascot was configured to search the Swiss-Prot database, assuming trypsin as the digestion enzyme. Database search against Mascot was performed with a fragment ion mass tolerance of 0.05 dalton and a parent ion tolerance of 25 ppm. Two missed cleavages were allowed during trypsin digestion. Oxidation (Met) and carbamidomethyl (Cys) and phosphorylation (STY) were specified as variable modification. Phosphorylation sites and peptide sequence assignments contained in Mascot search results were validated by manual confirmation from raw MS/MS data.

Database searching of cross-linking peptides

MassMatrix Database Search Engine was used to identify the potential cross-linked peptides with the input parameters similar to the one described previously (*49*). Trypsin was set as the enzyme used for digestion during sample preparation. Maximum number of missed cleavage allowed during proteolytic digestion was defined as 3. Carbamidomethyl of cysteines and oxidation of methionine residues were allowed as variable modifications. Mass error tolerance was 10.00 ppm for precursor peptide ions and 0.05 dalton for fragment ions. The quality of a peptide match was evaluated by pp, pp_2, and pp_{tag}. Minimum pp and pp_2 value of output was 5.3, and minimum pp_{tag} was 1.3. Maximum number of cross-links per peptide was 2. Cross-linking peptides were selected if the according peaks were presented in both the BS3-d_0 and BS3-d_4 MS spectra.

Downloaded from http://stke.sciencemag.org/ on February 5, 2015

Peptide synthesis

The monophosphorylated (MTGpYVVTRR) and dually phosphorylated p38γ peptide (MpTGpYVVTRR) were synthesized by the peptide synthesis laboratory at the Institute of Biological Chemistry, Academia Sinica. To neutralize the synthesized peptide, an arginine (R^{+5}) was introduced to the C terminus of the phosphopeptides. The purity of the peptides was determined to be >90% based on the results from high-performance liquid chromatography and MS analysis.

Crystallization and data collection

To cocrystallize the target protein with the phosphopeptide, a 10-fold molar excess of the dually phosphorylated p38γ peptide was added to the purified $N3PTP^{D811A/C842S}$ to a final concentration of 8.5 mg/ml. The crystals that were used for data collection of the phosphopeptide complex were grown using sitting drop vapor diffusion at 20°C from 1.5 μl of protein-peptide mixture and 0.5 μl of reservoir containing 100 mM tris-HCl (pH 8.5), 30% PEG-8000 (polyethylene glycol, molecular weight 800), and 5% glycerol. The crystal that was used for data collection of the $N3PTP^{C842S}$ mutant was grown in a condition similar to that used for the phosphopeptide complex, except that the reservoir contained 100 mM Hepes (pH 7.5) and 12% PEG-8000.

Before data collection, the phosphopeptide complex crystal was soaked in a cryoprotectant solution containing 100 mM tris-HCl (pH 8.5), 30% PEG-8000, and 6% glycerol. The $N3PTP^{C842}$ mutant crystal was soaked in a cryoprotectant solution containing 100 mM tris-HCl (pH 7.5), 12% PEG-8000, and 15% glycerol. X-ray diffraction data were collected at 100 K using the in-house x-ray source (wavelength 1.5 Å) and 15A1 beamline (wavelength 1.0 Å) at the National Synchrotron Radiation Research Center (Hsinchu City, Taiwan). Data were indexed, integrated, and scaled using HKL2000 (*50*).

Structure determination

The crystal structure of the $N3PTP^{C842S}$ mutant was determined by molecular replacement using Phaser (*51*) and the wild-type $PTPN3_{PTP}$ structure (PDB ID: 2B49) with the WPD loop region omitted as the search model. The best solution for the phosphopeptide complex structure was obtained using the $N3PTP^{C842S}$ mutant structure as the search model. Structure refinement was performed with PHENIX (*52*). TLS (translation-libration-screw) and riding hydrogens were included. Waters were added using the ordered solvent process and default parameters in PHENIX and were manually checked. The refined model was manually adjusted using Coot (*53*) guided by $F_o - F_c$ difference maps. The map revealed clear density for the residues 182 to 189 of the dually phosphorylated p38γ peptide. The quality and geometry of the refined structures were evaluated using MolProbity (*54*). Structural comparisons were performed with Dali (*55*), and figures of the structure were generated using PyMOL.

SAXS data collection and processing

The homogeneous solution of the $N3_{PTP}$–p-p38γ complex was characterized using the 23A1 small/wide angle x-ray scattering beamline at the National Synchrotron Radiation Research Center (Hsinchu City, Taiwan). Scattering data were collected at 15°C, with x-ray at a wavelength of λ = 0.8266 Å, and a sample-to-detector distance set at 2.5 m. Immediately before loading, the sample was centrifuged at 10,000*g* to remove large aggregates from the solution. For the collection, 50 μl of the complex sample solution was flowed past the x-ray beam at a rate of 4 μl/min, measuring seven frames each with a 30-s exposure. The sample solution scattering was averaged and corrected by the corresponding buffer solution scattering, and the data were plotted on absolute intensity scales by normalization against a water standard.

PRIMUS from the ATSAS version 2.5.2 was used for initial data evaluation (*56*, *57*). Kratky plot was used to assess the folded stat of the protein complex. The data quality was assessed by inspection of the linearity of the Guinier region of the data. The pair-distance distribution function [$p(r)$] was generated using GNOM (*58*), from which $I(0)$, R_g, and D_{max} were determined. The Porod volume was calculated by using the POROD function in PRIMUS, and the program DAMMIN (*21*) was used to generate 10 molecular SAXS envelopes of the $N3_{PTP}$–p-p38γ complex. These envelopes were averaged using DAMAVER (*59*). The online program FoXSDock (*22*) (http://modbase.compbio.ucsf.edu/foxsdock/) was used to generate the best-fit model using the PTP domain of the phosphopeptide complex structure and phospho-p38γ (PDB code: 1CM8) as the template. The predicted scattering profile of the best-fit model was verified using the program CRYSOL (*60*). The program SUPCOMB was used to align the best-fit model and SAXS-derived envelope (*61*).

Phosphatase assay and kinetic analysis

The phosphatase-catalyzed hydrolysis of phosphotyrosine-containing peptides was conducted using the monophosphorylated (MTGpYVVTRR) and the dually phosphorylated (MpTGpYVVTRR) p38γ peptides. To generate a 20 mM stock solution, the lyophilized powders of the phosphopeptides were dissolved in buffer containing 50 mM tris-HCl (pH 8.5), 50 mM NaCl.

To measure the phosphatase activity using phosphopeptides as substrates, 5 to 20 nM of purified PTPN3 constructs were added with 0 to 500 μM of the indicated phosphopeptide to a final volume of 200 μl, with assay buffer containing 50 mM tris-HCl (pH 7.4), 50 mM NaCl at 30°C. To measure the phosphatase activity using the purified phospho-p38γ as a substrate, 20 nM of wild-type N3PDZ-PTP or N3PTP was added with 0 to 50 μM phospho-p38γ to a final volume and buffer condition that was identical to the phosphopeptide assay. Various substrate concentrations and time points were used to calculate the enzyme kinetics. All of the reactions were terminated by adding 30 μl of phosphate reagent from the phosphate colorimetric assay kit (BioVision) following the manufacturer's instructions. The absorbance was measured at 650 nm using a PowerWave XS2 microplate reader (BioTeK), and the conversion of absorbance to the amount of phosphate production was calculated using a standard curve of known phosphate concentration. The data were fitted using a nonlinear curve, and the kinetics parameters K_m and K_{cat} were calculated from the Michaelis-Menten equation using Prism version 6.0d (GraphPad software). All of the points in the enzyme kinetics were measured in triplicate, and the experiments were repeated three times to obtain consistent results.

*p*NPP assay

The N3PDZ-PTP and N3PTP phosphatase assay using *p*NPP as the substrate was performed as previously described (*62*). In brief, 50 ng of purified wild-type N3PDZ-PTP or N3PTP was incubated in 50 μl of a solution containing 50 mM tris-HCl (pH 7.5), 50 mM NaCl, and 0 to 200 mM *p*NPP. The reactions were incubated for 1 to 15 min at 30°C and terminated by adding 100 μl of 1 M NaOH. The absorbance of the para-nitrophenol product was measured at 405 nm using a PowerWave XS2 microplate reader (BioTeK). All of the points were measured in triplicate, and the experiments were repeated three times.

Homology modeling

A homology model of N3PDZ (508 to 595) was constructed using the SWISS-MODEL Web server (*63*) (http://swissmodel.expasy.org/) with the PDZ domain of PTPN4 (PDB ID: 3NFK) as a template. HADDOCK was used to dock the PDZ and PTP domains of PTPN3 using a cross-linking–derived restraint. The PTP domain of the phosphopeptide

Downloaded from http://stke.sciencemag.org/ on February 5, 2015

complex structure and homology model of N3PDZ were used as starting templates. All of the docking steps were performed with the default setting on the easy interface of the HADDOCK Web server (*64*) (http://haddock.science.uu.nl/services/HADDOCK/). We measured the distance of the Cα atoms between Lys^{526} and Lys^{876} of the lowest-energy HADDOCK structure created in the docking run.

SUPPLEMENTARY MATERIALS

www.sciencesignaling.org/cgi/content/full/7/347/ra98/DC1
Fig. S1. MS spectra of p38γ phosphorylation.
Fig. S2. Activation of p38γ is required for the interaction with $N3PTP^{D811A/C842S}$.
Fig. S3. Superimposition of the wild-type N3PTP and phosphopeptide complex structures.
Fig. S4. Modeling of the phospho-p38γ activation loop from hidden to extended conformation.
Fig. S5. MS/MS spectra of intramolecular and intermolecular cross-linked peptides correspond to the linkage of N3PDZ-$PTP^{D811A/C842S}$ and phospho-p38γ.
Fig. S6. Homology model of N3PDZ.
Fig. S7. Cross-linking and MS derived $N3_{PDZ\text{-}PTP}$–p-p38γ complex using the best-fit model 2 of SAXS as template.
Fig. S8. Representative HADDOCK structures of N3PDZ-$PTP^{D811A/C842S}$ from each cluster.
Fig. S9. E-loop sequence alignment between FERM- and KIM-containing PTPs.
Table S1. Summary of protein constructs used in this study.
Table S2. SAXS data collection and analysis details.
Table S3. Comparison of SAXS-derived envelopes between different PTP-MAPK complexes.
Table S4. MS identification of cross-linked peptides between N3PDZ-$PTP^{D811A/C842S}$ and phospho-p38γ using BS3 cross-linker.
Table S5. MS identification of cross-linked peptides between $N3PTP^{D811A/C842S}$ and phospho-p38γ using BS3 cross-linker.
Table S6. MS identification of cross-linked peptides of N3PDZ-$PTP^{D811A/C842S}$ using BS3 cross-linker.
References (*66–70*)

REFERENCES AND NOTES

1. J. Downward, Targeting RAS signalling pathways in cancer therapy. *Nat. Rev. Cancer* **3**, 11–22 (2003).
2. A. M. Manning, R. J. Davis, Targeting JNK for therapeutic benefit: From junk to gold? *Nat. Rev. Drug Discov.* **2**, 554–565 (2003).
3. J. Han, P. Sun, The pathways to tumor suppression via route p38. *Trends Biochem. Sci.* **32**, 364–371 (2007).
4. M. Loesch, G. Chen, The p38 MAPK stress pathway as a tumor suppressor or more? *Front. Biosci.* **13**, 3581–3593 (2008).
5. D. Brancho, N. Tanaka, A. Jaeschke, J. J. Ventura, N. Kelkar, Y. Tanaka, M. Kyuuma, T. Takeshita, R. A. Flavell, R. J. Davis, Mechanism of p38 MAP kinase activation in vivo. *Genes Dev.* **17**, 1969–1978 (2003).
6. T. Zarubin, J. Han, Activation and signaling of the p38 MAP kinase pathway. *Cell Res.* **15**, 11–18 (2005).
7. J. Tang, X. Qi, D. Mercola, J. Han, G. Chen, Essential role of p38γ in K-Ras transformation independent of phosphorylation. *J. Biol. Chem.* **280**, 23910–23917 (2005).
8. X. M. Qi, N. M. Pohl, M. Loesch, S. W. Hou, R. S. Li, J. Z. Qin, A. Cuenda, G. Chen, P38α antagonizes p38γ activity through c-Jun-dependent ubiquitin-proteasome pathways in regulating ras transformation and stress response. *J. Biol. Chem.* **282**, 31398–31408 (2007).
9. X. M. Qi, J. Tang, M. Loesch, N. Pohl, S. Alkan, G. Chen, p38γ mitogen activated protein kinase integrates signaling crosstalk between Ras and estrogen receptor to increase breast cancer invasion. *Cancer Res.* **66**, 7540–7547 (2006).
10. M. Hasegawa, A. Cuenda, M. G. Spillantini, G. M. Thomas, V. Buée-Scherrer, P. Cohen, M. Goedert, Stress-activated protein kinase-3 interacts with the PDZ domain of α1-syntrophin. A mechanism for specific substrate recognition. *J. Biol. Chem.* **274**, 12626–12631 (1999).
11. S. W. Hou, H. Y. Zhi, N. Pohl, M. Loesch, X. M. Qi, R. S. Li, Z. Basir, G. Chen, PTPH1 dephosphorylates and cooperates with p38γ MAPK to increase Ras oncogenesis through PDZ-mediated interaction. *Cancer Res.* **70**, 2901–2910 (2010).
12. X. Qi, J. Tang, R. Pramanik, R. M. Schultz, S. Shirasawa, T. Sasazuki, J. Han, G. Chen, p38 MAPK activation selectively induces cell death in K-*ras*-mutated human colon cancer cells through regulation of vitamin D receptor. *J. Biol. Chem.* **279**, 22138–22144 (2004).
13. R. Pulido, A. Zúñiga, A. Ullrich, PTP-SL and STEP protein tyrosine phosphatases regulate the activation of the extracellular signal-regulated kinases ERK1 and ERK2 by association through a kinase interaction motif. *EMBO J.* **17**, 7337–7350 (1998).
14. M. Saxena, S. Williams, K. Taskén, T. Mustelin, Crosstalk between cAMP-dependent kinase and MAP kinase through a protein tyrosine phosphatase. *Nat. Cell Biol.* **1**, 305–311 (1999).
15. M. Camps, A. Nichols, S. Arkinstall, Dual specificity phosphatases: A gene family for control of MAP kinase function. *FASEB J.* **14**, 6–16 (2000).
16. A. J. Flint, T. Tiganis, D. Barford, N. K. Tonks, Development of "substrate-trapping" mutants to identify physiological substrates of protein tyrosine phosphatases. *Proc. Natl. Acad. Sci. U.S.A.* **94**, 1680–1685 (1997).
17. D. Barford, A. J. Flint, N. K. Tonks, Crystal structure of human protein tyrosine phosphatase 1b. *Science* **263**, 1397–1404 (1994).
18. T. Fox, M. J. Fitzgibbon, M. A. Fleming, H. M. Hsiao, C. L. Brummel, M. S. Su, Kinetic mechanism and ATP-binding site reactivity of p38γ MAP kinase. *FEBS Lett.* **461**, 323–328 (1999).
19. Z. Huang, B. Zhou, Z. Y. Zhang, Molecular determinants of substrate recognition in hematopoietic protein-tyrosine phosphatase. *J. Biol. Chem.* **279**, 52150–52159 (2004).
20. D. A. Critton, A. Tortajada, G. Stetson, W. Peti, R. Page, Structural basis of substrate recognition by hematopoietic tyrosine phosphatase. *Biochemistry* **47**, 13336–13345 (2008).
21. D. I. Svergun, Restoring low resolution structure of biological macromolecules from solution scattering using simulated annealing. *Biophys. J.* **76**, 2879–2886 (1999).
22. D. Schneidman-Duhovny, M. Hammel, A. Sali, Macromolecular docking restrained by a small angle X-ray scattering profile. *J. Struct. Biol.* **173**, 461–471 (2011).
23. S. Bellon, M. J. Fitzgibbon, T. Fox, H. M. Hsiao, K. P. Wilson, The structure of phosphorylated p38γ is monomeric and reveals a conserved activation-loop conformation. *Structure* **7**, 1057–1065 (1999).
24. A. White, C. A. Pargellis, J. M. Studts, B. G. Werneburg, B. T. Farmer II, Molecular basis of MAPK-activated protein kinase 2:p38 assembly. *Proc. Natl. Acad. Sci. U.S.A.* **104**, 6353–6358 (2007).
25. Y. G. Alevy, A. C. Patel, A. G. Romero, D. A. Patel, J. Tucker, W. T. Roswit, C. A. Miller, R. F. Heier, D. E. Byers, T. J. Brett, M. J. Holtzman, IL-13–induced airway mucus production is attenuated by MAPK13 inhibition. *J. Clin. Invest.* **122**, 4555–4568 (2012).
26. G. F. De Nicola, E. D. Martin, A. Chaikuad, R. Bassi, J. Clark, L. Martino, S. Verma, P. Sicard, R. Tata, R. A. Atkinson, S. Knapp, M. R. Conte, M. S. Marber, Mechanism and consequence of the autoactivation of p38α mitogen-activated protein kinase promoted by TAB1. *Nat. Struct. Mol. Biol.* **20**, 1182–1190 (2013).
27. Y. Y. Zhang, J. W. Wu, Z. X. Wang, Mitogen-activated protein kinase (MAPK) phosphatase 3-mediated cross-talk between MAPKs ERK2 and p38α. *J. Biol. Chem.* **286**, 16150–16162 (2011).
28. N. Babault, F. Cordier, M. Lafage, J. Cockburn, A. Haouz, C. Prehaud, F. A. Rey, M. Delepierre, H. Buc, M. Lafon, N. Wolff, Peptides targeting the PDZ domain of PTPN4 are efficient inducers of glioblastoma cell death. *Structure* **19**, 1518–1524 (2011).
29. Z. A. Chen, A. Jawhari, L. Fischer, C. Buchen, S. Tahir, T. Kamenski, M. Rasmussen, L. Lariviere, J. C. Bukowski-Wills, M. Nilges, P. Cramer, J. Rappsilber, Architecture of the RNA polymerase II–TFIIF complex revealed by cross-linking and mass spectrometry. *EMBO J.* **29**, 717–726 (2010).
30. C. Schmidt, M. Zhou, H. Marriott, N. Morgner, A. Politis, C. V. Robinson, Comparative cross-linking and mass spectrometry of an intact F-type ATPase suggest a role for phosphorylation. *Nat. Commun.* **4**, 1985 (2013).
31. C. Dominguez, R. Boelens, A. M. Bonvin, HADDOCK: A protein–protein docking approach based on biochemical or biophysical information. *J. Am. Chem. Soc.* **125**, 1731–1737 (2003).
32. S. J. de Vries, A. D. van Dijk, M. Krzeminski, M. van Dijk, A. Thureau, V. Hsu, T. Wassenaar, A. M. Bonvin, HADDOCK versus HADDOCK: New features and performance of HADDOCK2.0 on the CAPRI targets. *Proteins* **69**, 726–733 (2007).
33. D. Pei, U. Lorenz, U. Klingmüller, B. G. Neel, C. T. Walsh, Intramolecular regulation of protein tyrosine phosphatase SH-PTP1: A new function for Src homology 2 domains. *Biochemistry* **33**, 15483–15493 (1994).
34. D. A. Critton, L. Tautz, R. Page, Visualizing active-site dynamics in single crystals of HePTP: Opening of the WPD loop involves coordinated movement of the E loop. *J. Mol. Biol.* **405**, 619–629 (2011).
35. T. A. Millward, S. Zolnierowicz, B. A. Hemmings, Regulation of protein kinase cascades by protein phosphatase 2A. *Trends Biochem. Sci.* **24**, 186–191 (1999).
36. B. Zhou, Z. X. Wang, Y. Zhao, D. L. Brautigan, Z. Y. Zhang, The specificity of extracellular signal-regulated kinase 2 dephosphorylation by protein phosphatases. *J. Biol. Chem.* **277**, 31818–31825 (2002).
37. K. Kullander, R. Klein, Mechanisms and functions of eph and ephrin signalling. *Nat. Rev. Mol. Cell Biol.* **3**, 475–486 (2002).
38. E. B. Pasquale, Eph-ephrin bidirectional signaling in physiology and disease. *Cell* **133**, 38–52 (2008).
39. A. Palmer, M. Zimmer, K. S. Erdmann, V. Eulenburg, A. Porthin, R. Heumann, U. Deutsch, R. Klein, EphrinB phosphorylation and reverse signaling: Regulation by Src kinases and PTP-BL phosphatase. *Mol. Cell* **9**, 725–737 (2002).
40. S. R. Kumar, J. S. Scehnet, E. J. Ley, J. Singh, V. Krasnoperov, R. Liu, P. K. Manchanda, R. D. Ladner, D. Hawes, F. A. Weaver, R. W. Beart, G. Singh, C. Nguyen, M. Kahn, P. S. Gill, Preferential induction of EphB4 over EphB2 and its implication in colorectal cancer progression. *Cancer Res.* **69**, 3736–3745 (2009).

Downloaded from http://stke.sciencemag.org/ on February 5, 2015

41. N. I. Herath, M. D. Spanevello, J. D. Doecke, F. M. Smith, C. Pouponnot, A. W. Boyd, Complex expression patterns of Eph receptor tyrosine kinases and their ephrin ligands in colorectal carcinogenesis. *Eur. J. Cancer* **48**, 753–762 (2012).
42. N. Krishnan, D. Koveal, D. H. Miller, B. Xue, S. D. Akshinthala, J. Kragelj, M. R. Jensen, C. M. Gauss, R. Page, M. Blackledge, S. K. Muthuswamy, W. Peti, N. K. Tonks, Targeting the disordered C terminus of PTP1B with an allosteric inhibitor. *Nat. Chem. Biol.* **10**, 558–566 (2014).
43. L. Stols, M. Gu, L. Dieckman, R. Raffen, F. R. Collart, M. I. Donnelly, A new vector for high-throughput, ligation-independent cloning encoding a tobacco etch virus protease cleavage site. *Protein Expr. Purif.* **25**, 8–15 (2002).
44. K. E. Chen, A. A. Richards, T. T. Caradoc-Davies, P. R. Vajjhala, G. Robin, L. H. Lua, J. M. Hill, K. Schroder, M. J. Sweet, S. Kellie, B. Kobe, J. Martin, The structure of the caspase recruitment domain of BinCARD reveals that all three cysteines can be oxidized. *Acta Crystallogr. D Biol. Crystallogr.* **69**, 774–784 (2013).
45. A. J. Barr, E. Ugochukwu, W. H. Lee, O. N. King, P. Filippakopoulos, I. Alfano, P. Savitsky, N. A. Burgess-Brown, S. Muller, S. Knapp, Large-scale structural analysis of the classical human protein tyrosine phosphatome. *Cell* **136**, 352–363 (2009).
46. D. Hayes, T. M. Laue, J. Philo, *Program Sednterp: Sedimentation Interpretation Program* (University of New Hampshire, Durham, NH, 1995).
47. P. Schuck, Size-distribution analysis of macromolecules by sedimentation velocity ultracentrifugation and Lamm equation modeling. *Biophys. J.* **78**, 1606–1619 (2000).
48. K. E. Chen, A. A. Richards, J. K. Ariffin, I. L. Ross, M. J. Sweet, S. Kellie, B. Kobe, J. L. Martin, The mammalian DUF59 protein Fam96a is enriched in macrophages and forms two distinct types of domain-swapped dimer. *Acta Crystallogr. D Biol. Crystallogr.* **68**, 637–648 (2012).
49. Y. Gordiyenko, C. Schmidt, M. D. Jennings, D. Matak-Vinkovic, G. D. Pavitt, C. V. Robinson, eIF2B is a decameric guanine nucleotide exchange factor with a $\gamma_2\epsilon_2$ tetrameric core. *Nat. Commun.* **5**, 3902 (2014).
50. Z. Otwinowski, W. Minor, Processing of X-ray diffraction data collected in oscillation mode. *Methods Enzymol.* **276**, 307–326 (1997).
51. A. J. McCoy, R. W. Grosse-Kunstleve, P. D. Adams, M. D. Winn, L. C. Storoni, R. J. Read, Phaser crystallographic software. *J. Appl. Crystallogr.* **40**, 658–674 (2007).
52. P. D. Adams, P. V. Afonine, G. Bunkóczi, V. B. Chen, I. W. Davis, N. Echols, J. J. Headd, L. W. Hung, G. J. Kapral, R. W. Grosse-Kunstleve, A. J. McCoy, N. W. Moriarty, R. Oeffner, R. J. Read, D. C. Richardson, J. S. Richardson, T. C. Terwilliger, P. H. Zwart, PHENIX: A comprehensive Python-based system for macromolecular structure solution. *Acta Crystallogr. D Biol. Crystallogr.* **66**, 213–221 (2010).
53. P. Emsley, K. Cowtan, *Coot*: Model-building tools for molecular graphics. *Acta Crystallogr. D Biol. Crystallogr.* **60**, 2126–2132 (2004).
54. V. B. Chen, W. B. Arendall III, J. J. Headd, D. A. Keedy, R. M. Immormino, G. J. Kapral, L. W. Murray, J. S. Richardson, D. C. Richardson, *MolProbity*: All-atom structure validation for macromolecular crystallography. *Acta Crystallogr. D Biol. Crystallogr.* **66**, 12–21 (2010).
55. L. Holm, P. Rosenström, Dali server: Conservation mapping in 3D. *Nucleic Acids Res.* **38**, W545–W549 (2010).
56. M. V. Petoukhov, D. Franke, A. V. Shkumatov, G. Tria, A. G. Kikhney, M. Gajda, C. Gorba, H. D. T. Mertens, P. V. Konarev, D. I. Svergun, New developments in the *ATSAS* program package for small-angle scattering data analysis. *J. Appl. Cryst.* **45**, 342–350 (2012).
57. P. V. Konarev, V. V. Volkov, A. V. Sokolova, M. H. J. Koch, D. I. Svergun, PRIMUS: A Windows PC-based system for small-angle scattering data analysis. *J. Appl. Cryst.* **36**, 1277–1282 (2003).
58. D. I. Svergun, Determination of the regularization parameter in indirect-transform methods using perceptual criteria. *J. Appl. Cryst.* **25**, 495–503 (1992).
59. V. V. Volkov, D. I. Svergun, Uniqueness of ab initio shape determination in small-angle scattering. *J. Appl. Cryst.* **36**, 860–864 (2003).
60. D. Svergun, C. Barberato, M. H. J. Koch, CRYSOL—A program to evaluate x-ray solution scattering of biological macromolecules from atomic coordinates. *J. Appl. Cryst.* **28**, 768–773 (1995).
61. M. B. Kozin, D. I. Svergun, Automated matching of high- and low-resolution structural models. *J. Appl. Cryst.* **34**, 33–41 (2001).
62. M. F. Hsu, T. C. Meng, Enhancement of insulin responsiveness by nitric oxide-mediated inactivation of protein-tyrosine phosphatases. *J. Biol. Chem.* **285**, 7919–7928 (2010).
63. K. Arnold, L. Bordoli, J. Kopp, T. Schwede, The SWISS-MODEL workspace: A web-based environment for protein structure homology modelling. *Bioinformatics* **22**, 195–201 (2006).
64. S. J. de Vries, M. van Dijk, A. M. Bonvin, The HADDOCK web server for data-driven biomolecular docking. *Nat. Protoc.* **5**, 883–897 (2010).
65. J. V. Staros, P. S. Anjaneyulu, Membrane-impermeant cross-linking reagents. *Methods Enzymol.* **172**, 609–628 (1989).
66. C. Combet, C. Blanchet, C. Geourjon, G. Deléage, NPS@: Network protein sequence analysis. *Trends Biochem. Sci.* **25**, 147–150 (2000).
67. D. M. Francis, B. Różycki, A. Tortajada, G. Hummer, W. Peti, R. Page, Resting and active states of the ERK2:HePTP complex. *J. Am. Chem. Soc.* **133**, 17138–17141 (2011).
68. D. M. Francis, G. S. Kumar, D. Koveal, A. Tortajada, R. Page, W. Peti, The differential regulation of p38α by the neuronal kinase interaction motif protein tyrosine phosphatases, a detailed molecular study. *Structure* **21**, 1612–1623 (2013).
69. D. M. Francis, B. Różycki, D. Koveal, G. Hummer, R. Page, W. Peti, Structural basis of p38α regulation by hematopoietic tyrosine phosphatase. *Nat. Chem. Biol.* **7**, 916–924 (2011).
70. D. M. Francis, D. Koveal, A. Tortajada, R. Page, W. Peti, Interaction of kinase-interaction-motif protein tyrosine phosphatases with the mitogen-activated protein kinase ERK2. *PLOS One* **9**, e91934 (2014).

Acknowledgments: We would like to thank Y.-L. Huang of the Institute of Biological Chemistry for the peptide synthesis. We also thank National Core Facility for Protein Structural Analysis for crystallization screening. LC-MS/MS spectra were acquired at the Academia Sinica Common Mass Spectrometry Facilities of the Institute of Biological Chemistry. X-ray data were collected on the in-house x-ray source and 15A1 beamlines at the National Synchrotron Radiation Research Center, Taiwan. **Funding:** This research was supported by grants from the Institute of Biological Chemistry at Academia Sinica and National Program for Biopharmaceuticals (NRPB, NSC 10102325-B-492-001). **Author contributions:** K.-E.C. designed and conducted all experiments, analyzed the data, and wrote the paper. S.-Y.L., M.-J.W., M.-R.H., A.S., and C.-C.C. performed some experiments and analyzed the data. T.-C.M. and A.H.-J.W. directed the research and wrote the paper. **Competing interests:** The authors declare that they have no competing financial interests. **Data and materials availability:** The atomic coordinates have been deposited in the Protein Data Bank as PDB ID: 4QUM and PDB ID: 4QUN.

Submitted 21 July 2014
Accepted 24 September 2014
Final Publication 14 October 2014
10.1126/scisignal.2005722
Citation: K.-E. Chen, S.-Y. Lin, M.-J. Wu, M.-R. Ho, A. Santhanam, C.-C. Chou, T.-C. Meng, A. H.-J. Wang, Reciprocal allosteric regulation of p38γ and PTPN3 involves a PDZ domain–modulated complex formation. *Sci. Signal.* **7**, ra98 (2014).

Downloaded from http://stke.sciencemag.org/ on February 5, 2015

Science Signaling
AAAS

Reciprocal allosteric regulation of p38γ and PTPN3 involves a PDZ domain–modulated complex formation

Kai-En Chen, Shu-Yu Lin, Mei-Ju Wu, Meng-Ru Ho, Abirami Santhanam, Chia-Cheng Chou, Tzu-Ching Meng and Andrew H. -J. Wang (October 14, 2014)

Science Signaling 7 (347), ra98. [doi: 10.1126/scisignal.2005722]

The following resources related to this article are available online at http://stke.sciencemag.org. This information is current as of February 5, 2015.

Article Tools Visit the online version of this article to access the personalization and article tools:
http://stke.sciencemag.org/content/7/347/ra98

Supplemental Materials *"Supplementary Materials"*
http://stke.sciencemag.org/content/suppl/2014/10/09/7.347.ra98.DC1.html

Related Content The editors suggest related resources on *Science*'s sites:
http://stke.sciencemag.org/content/sigtrans/4/204/pe47.full.html
http://stke.sciencemag.org/content/sigtrans/5/226/eg7.full.html
http://stke.sciencemag.org/content/sigtrans/4/204/ra88.full.html
http://stke.sciencemag.org/content/sigtrans/7/347/pc28.full.html

References This article cites 69 articles, 20 of which you can access for free at:
http://stke.sciencemag.org/content/7/347/ra98#BIBL

Glossary Look up definitions for abbreviations and terms found in this article:
http://stke.sciencemag.org/cgi/glossarylookup

Permissions Obtain information about reproducing this article:
http://www.sciencemag.org/about/permissions.dtl

Science Signaling (ISSN 1937-9145) is published weekly, except the last December, by the American Association for the Advancement of Science, 1200 New York Avenue, NW, Washington, DC 20005. Copyright 2015 by the American Association for the Advancement of Science; all rights reserved.

Downloaded from http://stke.sciencemag.org/ on February 5, 2015